



Unifying Charge Generation, Recombination, and Extraction in Low-Offset Non-Fullerene Acceptor Organic Solar Cells

Akchheta Karki, Joachim Vollbrecht, Alexander J. Gillett, Philipp Selter, Jaewon Lee, Zhengxing Peng, Nora Schopp, Alana L. Dixon, Max Schrock, Vojtech Nádaždy, Franz Schauer, Harald Ade, Bradley F. Chmelka, Guillermo C. Bazan, Richard H. Friend, and Thuc-Quyen Nguyen*

Even though significant breakthroughs with over 18% power conversion efficiencies (PCEs) in polymer:non-fullerene acceptor (NFA) bulk heterojunction organic solar cells (OSCs) have been achieved, not many studies have focused on acquiring a comprehensive understanding of the underlying mechanisms governing these systems. This is because it can be challenging to delineate device photophysics in polymer:NFA blends comprehensively, and even more complicated to trace the origins of the differences in device photophysics to the subtle differences in energetics and morphology. Here, a systematic study of a series of polymer:NFA blends is conducted to unify and correlate the cumulative effects of i) voltage losses, ii) charge generation efficiencies, iii) non-geminate recombination and extraction dynamics, and iv) nuanced morphological differences with device performances. Most importantly, a deconvolution of the major loss processes in polymer:NFA blends and their connections to the complex BHJ morphology and energetics are established. An extension to advanced morphological techniques, such as solid-state NMR (for atomic level insights on the local ordering and donor:acceptor π - π interactions) and resonant soft X-ray scattering (for donor and acceptor interfacial area and domain spacings), provide detailed insights on how efficient charge generation, transport, and extraction processes can outweigh increased voltage losses to yield high PCEs.

1. Introduction

A significant leap in record-breaking power conversion efficiencies (PCEs) of single-junction bulk-heterojunction (BHJ) organic solar cells (OSCs) to over 18%^[1] has recently been achieved. This can be credited to the rapid developments of new non-fullerene acceptors (NFAs) paired with suitable high performing polymer donors. While these breakthroughs are encouraging, it remains crucial to attain a deeper and more comprehensive understanding of the underlying mechanisms governing these novel and high performing polymer:NFA systems. Several recent studies have attributed the high performances of NFA-based solar cells to an improvement in the open-circuit voltage (V_{OC}) without significantly diminishing the charge generation efficiency.^[2-4] Particularly, in polymer:NFA systems, high V_{OC} values have been achieved with efficient charge generation regardless of a very small energetic driving force for

A. Karki, Dr. J. Vollbrecht, N. Schopp, A. L. Dixon, M. Schrock, Prof. G. C. Bazan, Prof. T.-Q. Nguyen
Center for Polymers and Organic Solids
University of California Santa Barbara (UCSB)
Santa Barbara, CA 93106, USA
E-mail: quyen@chem.ucsb.edu

Dr. A. J. Gillett, Prof. R. H. Friend
Optoelectronics Group Cavendish Laboratory
University of Cambridge
J. J. Thomson Avenue, Cambridge CB3 0HE, UK
Dr. P. Selter, Prof. B. F. Chmelka
Department of Chemical Engineering
University of California Santa Barbara (UCSB)
Santa Barbara, CA 93106, USA

The ORCID identification number(s) for the author(s) of this article can be found under <https://doi.org/10.1002/aenm.202001203>.

Prof. J. Lee
Department of Chemical Engineering and Applied Chemistry
Chungnam National University
Daejeon 34134, Republic of Korea

Z. Peng, Prof. H. Ade
Department of Physics and Organic and Carbon Electronics Lab (ORaCEL)
North Carolina State University
Raleigh, NC 27695, USA

Dr. V. Nádaždy
Institute of Physics
SAS
Centre for Advanced Material Application
SAS
Dubravská cesta 9, Bratislava 845 11, Slovak Republic

Prof. F. Schauer
Tomas Bata University in Zlín
Nad Stráněmi 4511, Zlín CZ 760 05, Czech Republic

DOI: 10.1002/aenm.202001203

exciton dissociation (ΔG_{S_1-CT}), where ΔG_{S_1-CT} is defined as the energy difference between the charge-transfer (CT) state and singlet-exciton (S_1) state of the lower bandgap component in the blend. While blend systems with low energetic offsets are sought for achieving high V_{OC} values, such blends commonly suffer from modest short-circuit current (J_{SC}) and fill-factor (FF) values, which can limit the PCE.^[5–8] This compromise between V_{OC} , J_{SC} , and FF has been observed in numerous recently reported systems, and was more commonly found in polymer:fullerene blends.^[5–9] However, of late, some reported high performing polymer:NFA blends have managed to optimally balance this tradeoff and achieve PCEs ranging from 10–18%.^[5,10–15] Therefore, attaining a deeper understanding of the charge generation dynamics in conjunction with a study of the voltage losses in blends with low energetic offsets has become crucial. Besides an understanding of the aforementioned processes, non-geminate recombination and charge extraction dynamics are the other important parameters needed to understand the delicate interplay between V_{OC} , FF, and J_{SC} . Non-geminate recombination has been shown to be the dominant loss process in most high performing non-fullerene acceptor BHJ OSCs.^[4,16–20] As a consequence, reducing non-geminate recombination would give rise to an overall improved device performance. Non-geminate recombination occurs when free electrons and holes originating from different excitons meet and recombine. In competition with the non-geminate recombination process is charge extraction. It has been shown that if the charge extraction time (τ_{ex}) is faster than or comparable to the recombination time (τ_{rec}), then charge recombination can be curtailed, and FF and J_{SC} values can be improved.^[6,21,22] Concomitant with all these processes is the morphology of the BHJ blend that warrants an in-depth investigation due to its direct impact on the charge generation, recombination, and extraction processes.^[6,11,21] In this work, morphological investigations that include solid-state(ss)-NMR (for insights on D:A interactions and local atomic-level ordering)^[23] and resonant-soft x-ray scattering (RSOXS) (for the D:A interfacial area and domain spacings)^[24] provide a detailed picture of how donor (D) and acceptor (A) molecules pack in polymer:NFA BHJ blends offering insights on the connections between device photo-physics and morphology.

We begin by systematically varying the S_1 -CT offsets for a series of polymer:NFA blend systems by fluorinating the IOTIC-based NFAs. The cumulative effect is investigated by systematically tuning the S_1 -CT offset for a series of polymer:NFA systems on the i) voltage losses, ii) charge generation efficiencies, iii) non-geminate recombination and extraction dynamics, and iv) D:A interfacial area, short-range atomic-level (nm to sub-nm) ordering and interactions. As a result, a quantitative understanding of the charge dynamics that starts at photoexcitation and ends at charge extraction has not been attained for a series of polymer:NFA blends with systematically fluorinated NFAs. The effect of fluorinating NFAs is known to be a widely used method to enhance photovoltaic device performances in polymer:NFA blends.^[5,25–30] However, because of the structural similarity in the NFAs used, it becomes rather challenging to identify the molecular level origins of this subtle change in molecular structure and its consequent impact on device performances. In fact, while

there are several studies in the literature that have utilized ssNMR to characterize blend morphologies for polymers or polymer:fullerene blends,^[23,31–37] the application of ssNMR techniques to characterize structurally similar polymer:NFA blends is limited.^[11,38] While fluorination in conjugated systems has been shown to result in improved molecular level interactions and charge transport by many previous reports,^[29,39–41] this is the first time that crucial differences such as π - π interactions and local ordering in polymer:NFA blends could also be resolved via ssNMR. Here, we posit that low energetic offset polymer:NFA systems with low voltage losses are key in attaining high PCEs—but not without a caveat. The drawbacks brought forth by low energetic offset systems can only be circumvented with a comprehensive understanding of the charge generation, recombination, and extraction dynamics, as well as a further deconvolution of the role of the nuanced differences in the BHJ morphology in these specific processes. Hence, from this systematic work, we uncover the genuine effects of changing the energetic offsets on the tradeoffs between V_{OC} , FF, and J_{SC} of the studied blend systems.

2. Results and Discussions

2.1. Chemical Structures and Energy Levels of Donor and Acceptors

Figure 1 shows the energy levels and chemical structures of the polymer donor and NFAs used in this study. The PTB7-Th donor polymer was used in conjunction with a series of non-fullerene -based acceptors. The IEICO and IEICO-4F NFAs first reported in previous studies^[30,42] are used in this study, along with the IOTIC-2F NFA consisting of different isomeric ratios compared to the molecule previously reported in literature.^[43] For consistency in naming across the three NFAs, the IEICO and IEICO-4F NFAs will be referred as IOTIC and IOTIC-4F, respectively, in the scope of this study. Due to the variation in the isomeric ratios of the NFA (Table S1, Supporting Information), the IOTIC-2F NFA will be referred to as IOTIC-2F_a. Therefore, we will be investigating the performance of the PTB7-Th donor with the IOTIC, IOTIC-2F_a, and IOTIC-4F NFAs. The consecutive additions of two fluorine atoms on the IOTIC-based acceptors (2- and 4- fluorine atoms) causes the highest occupied molecular orbital (HOMO) of the acceptors to be deeper leading to larger energetic offsets. For a consistent comparison of the three blends, conventional devices with a PEDOT:PSS layer as the bottom contact and evaporated barium capped with aluminum electrodes as the top contact were used.

2.2. Photovoltaic Performance

Figure 2a shows the J - V curves at 1 sun illumination (100 mW cm⁻², AM 1.5) of the three optimized blend systems. The average PCE values from 30 devices for each blend system are included in Table 1. The three representative J - V curves show that with a decrease in the energetic offsets (i.e., from

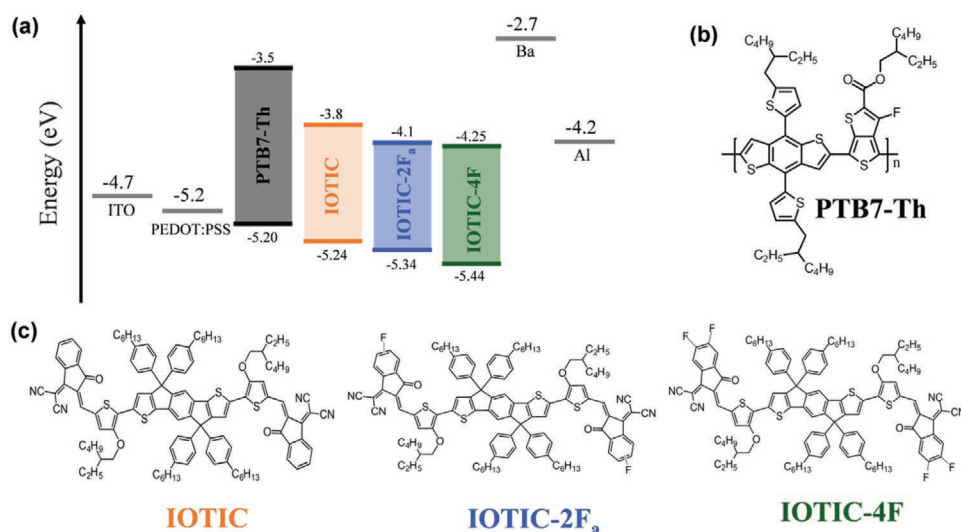


Figure 1. a) Energy levels of materials used obtained by cyclic voltammetry and chemical structures of b) PTB7-Th donor and c) IOTIC, IOTIC-2F_a, and IOTIC-4F NFAs.

PTB7-Th:IOTIC-4F to PTB7-Th:IOTIC), there is an increase in the V_{OC} values from 0.72 to 0.88 V and a concomitant decrease in the J_{SC} values from 20.5 to 10.7 mA cm⁻² of the devices. Decent FF values above 60% are retained in all three systems, with the PTB7-Th:IOTIC-4F blend system exhibiting the highest FF of 68%. Integrated J_{SC} values from external quantum efficiency (EQE) spectra of all three blend systems are within 4% of the average J_{SC} values measured via the $J-V$ characteristics of the devices at 1 sun illumination (Table 1). A combined simulation and experimental approach^[44] was used to obtain the internal quantum efficiencies (IQEs) for all three blend systems. The IQE is defined as the ratio of the number of charge carriers extracted from the device to the number of photons absorbed in the active layer. Therefore, IQE measurements provide useful information about the electrical properties of a device that EQE measurements alone cannot.^[44] Here, differences in the IQEs of the three blends suggest decreased charge generation efficiency and extraction upon going from the PTB7-Th:IOTIC-4F to the PTB7-Th:IOTIC blend system (Figure 2b).

To ensure that all three blend systems were pertinent for a systematic comparative study, the solar cells were first tested

under varying light intensities (I) to qualitatively determine the dominant type of non-geminate recombination mechanism by measuring the light intensity dependence of the V_{OC} (Figure S2, Supporting Information).^[45,46] The light intensities were decreased by neutral density filters and the V_{OC} versus $\ln(I)$ plots exhibited a slope of $s \approx 1 kT/q$ for all three blends, where k is the Boltzmann constant, T is the absolute temperature, and q is the elementary charge. To ensure that the effect of leakage current did not contribute to (increase) the slopes of the V_{OC} versus $\ln(I)$ plots,^[47] the dark $J-V$ curves at different light intensities were plotted and analyzed (Figure S3, Supporting Information). Additionally, literature reports have suggested the effects of non-ohmic contacts that may hinder charge collection efficiencies on the light intensity dependence of V_{OC} . Any issues arising from the collection efficiency as a result of using barium as an interlayer should be reflected on the V_{OC} versus $\ln(I)$ plots where the V_{OC} should saturate at higher intensities and show lower slopes than kT/q , rather than a slope of kT/q (suggesting dominant bimolecular recombination processes). Since all three blend systems show slopes of kT/q with no obvious saturation at higher intensities, we can confirm that

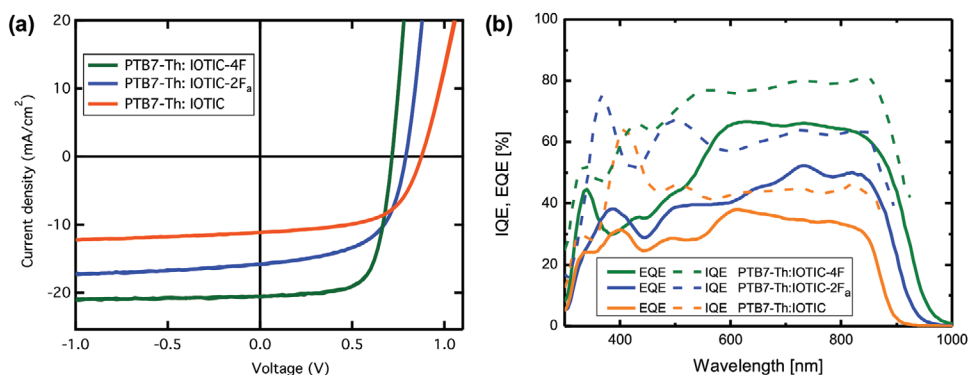


Figure 2. a) $J-V$ curves at 1 sun illumination (100 mW cm⁻², AM 1.5) and b) EQE and IQE spectra of the three blend films.

Table 1. Average PCEs obtained at 1 sun illumination (100 mW cm⁻², AM 1.5) from 30 devices for each blend system.

| Blend system | V _{OC} [V] | J _{SC} [mA cm ⁻²] | Integrated J _{SC} from EQE [mA cm ⁻²] | FF | PCE _{max} (PCE _{avg}) [%] |
|-------------------------------|---------------------|--|--|-------------|--|
| PTB7-Th:IOTIC-4F | 0.72 ± 0.002 | 20.5 ± 0.5 | 19.7 | 0.68 ± 0.02 | 10.2 (10.1 ± 0.2) |
| PTB7-Th:IOTIC-2F _a | 0.79 ± 0.003 | 14.8 ± 0.7 | 14.5 | 0.60 ± 0.02 | 7.2 (7.0 ± 0.2) |
| PTB7-Th:IOTIC | 0.88 ± 0.003 | 10.7 ± 0.5 | 10.3 | 0.60 ± 0.01 | 6.0 (5.7 ± 0.3) |

the collection efficiency of the devices is not compromised. To illustrate this point further, the V_{OC} versus ln(I) plots of a device consisting of just aluminum (a non-ohmic contact) is now included in Figure S4, Supporting Information. In this case, as a result of the saturation of the V_{OC} values at higher light intensities, slopes of less than kT/q were observed. The V_{OC} versus ln(I) plots were further measured at temperatures ranging from 200 to 300 K. Remarkably, all three blend systems showed $s \approx 1 kT/q$ at all temperatures in the range of 200–300 K, suggesting dominant bimolecular recombination mechanism processes (Figure S5, Supporting Information). Evaluating the temperature dependence behavior of V_{OC} versus ln(I) plots are often neglected in the literature, however, its importance has been highlighted by Koster et al.^[45] for confirming the dominant recombination loss processes. Such a confirmation is especially important for a comparison of the three blend systems chosen for this systematic study, as variations in the dominant recombination mechanisms; for example, the presence of trap assisted recombination could lead to an inconsistent comparison of the three blend systems.

2.3. Quantifying Voltage Losses

To quantify the voltage losses that limit the V_{OC} in the three blends, we evaluate the energy loss, E_{loss} as

$$E_{\text{loss}} = S_1 - qV_{\text{OC}} \quad (1)$$

where, S₁ is the singlet exciton energy of the lower bandgap component in the blend and q is the elementary charge. For a precise measurement of the singlet exciton energy of the lower bandgap components in the blends, we use the optical method described by Vandewal et al.^[48] (Figure S6, Supporting Information). The S₁ states of the three blend systems are also shown in the energy loss diagram depicted in **Figure 3**. To obtain the S₁, the intersection points of the emission spectra (from electroluminescence measurements, EL) and absorption spectra (from photovoltaic EQE measurements, EQE_{PV}) of the lower bandgap components in the blends (NFAs: IOTIC, IOTIC-2F_a, IOTIC-4F) were determined. From this analysis, it was found that upon fluorination, the IOTIC-based NFAs show a decrease in the S₁ from 1.44 eV (IOTIC) to 1.36 eV (IOTIC-2F_a) to 1.34 eV (IOTIC-4F).

Losses limiting the V_{OC} can be further divided into two parts: losses due to charge transfer as defined by the difference between the S₁ and the energy of the CT state (E_{CT}), and losses due to recombination and energetic disorder defined by the differences in E_{CT} and V_{OC}. Commonly, to identify the CT state in a blend, the EQE_{PV} is measured, and the CT state is identified as the absorption feature visible at energies lower than the bandgap of either the donor or the acceptor. The E_{CT} is

then determined by fitting an expression derived from Marcus theory (Equation S1, Supporting Information) to the tail of the blend EQE_{PV} spectrum.^[49] However, the CT state is not always pronounced in the low-energy tail of the EQE_{PV} spectra, especially in blends where the energetic offsets between the donor and acceptor are low (i.e., low HOMO-HOMO or LUMO-LUMO offsets),^[5,8,14,50] and so it can be difficult to distinguish the energy of the CT state from the donor or acceptor singlet state. It is possible, however, to significantly reduce the degrees of freedom in the fitting by 1) performing a simultaneous fit to both the EQE_{PV} (S1, Supporting Information) and the EL (Equation S2, Supporting Information) spectra^[3,9,11,51–53] using equations derived from Marcus theory, as was first demonstrated by Vandewal et al.^[49] and 2) calculating the EQE_{PV} down to values on the order of 10⁻⁷ using sensitively measured EL data and the reciprocity relationship shown in Equation S3, Supporting Information.^[54] In all three blend systems, the added sensitivity of up to four orders of magnitude with the calculated EQE_{PV} data (Equation S3, Supporting Information) from the reciprocity relationship allows for a better deconvolution of the Gaussian-shaped CT absorption which was previously absent from the sharp absorption tail of the measured EQE_{PV} data (Figure S7, Supporting Information). From such an analysis, the E_{CT} values in the three blend films were estimated to be 1.390, 1.295, and 1.260 eV for PTB7-Th:IOTIC, PTB7-Th:IOTIC-2F_a, and PTB7-Th:IOTIC-4F, respectively. It is worth noting that despite the reduction in degrees of freedom in the Marcus fitting, the E_{CT} values obtained here serve only as an estimate, due to the significant uncertainty that arises in separating the CT state emission and the singlet exciton emission in low energetic offset systems. Therefore, we report the CT energy in this blend—as has been done in some recently reported papers^[9,11,53,55]—with a caveat that the obtained E_{CT} value is an estimate only.

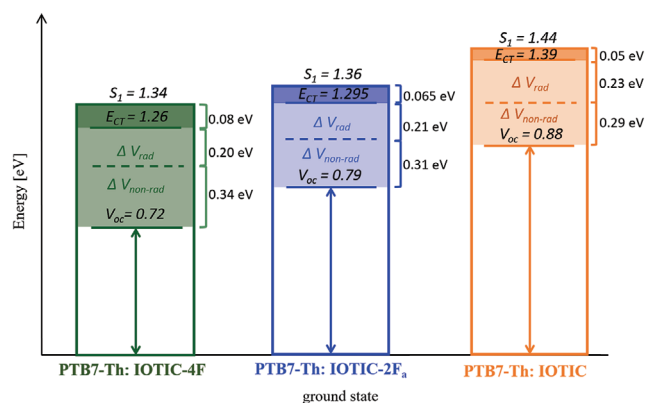


Figure 3. Energy loss diagrams of the three studied blend systems from S₁ to V_{OC}.

Table 2. Summarizing energy losses from S_1 to V_{OC} for all three blends. S_1 is determined from the intersection of the EL and EQE of the narrower bandgap components (acceptors) in the blends, E_{CT} is obtained via simultaneous fitting to the reduced emission and absorption spectrum using Marcus theory and the trends in E_{CT} are confirmed with temperature dependent V_{OC} method, ΔV_{rad} is obtained from Equation S5, Supporting Information, the calculated $\Delta V_{non-rad}$ is obtained from Equations S4 and S5, Supporting Information, and the experimental $\Delta V_{non-rad}$ is obtained from EQE_{EL} measurements (Equation S6, Supporting Information).

| Blend system | S_1 [eV] | E_{CT} [eV] | ΔV_{rad} [eV] | $\Delta V_{non-rad, calc}$ [eV] | $\Delta V_{non-rad, exp}$ [eV] | V_{OC} [V] |
|-------------------------------|------------|---------------|-----------------------|---------------------------------|--------------------------------|--------------|
| PTB7-Th:IOTIC | 1.44 | 1.39 | 0.227 | 0.283 | 0.290 | 0.88 |
| PTB7-Th:IOTIC-2F _a | 1.36 | 1.295 | 0.212 | 0.298 | 0.305 | 0.792 |
| PTB7-Th:IOTIC-4F | 1.34 | 1.26 | 0.203 | 0.337 | 0.338 | 0.716 |

Nevertheless, due to the uncertainty in the absolute values of the obtained CT energies, we adopt the temperature-dependent V_{OC} method as a second technique to further corroborate the trends of the measured E_{CT} values at room temperature of the three blend systems (Figure S8, Supporting Information). It has been shown that the extrapolation of temperature-dependent V_{OC} conducted at different light intensities to 0 K corresponds to the E_{CT} value at 0 K.^[49] Since the E_{CT} values exhibit some temperature dependence, the values at 0 K will be lower than the values measured at room temperature.^[49,56,57] The similar variation in the E_{CT} values between the three blend systems of ≈ 130 meV at both room temperature and 0 K can be used to verify—if not the absolute values—at least the trends in the E_{CT} values measured at room temperature (Table S1, Supporting Information).^[57] From such an analysis, a rough estimate of the energetic offsets (ΔG_{S_1-CT}) in these systems can now be determined. The PTB7-Th:IOTIC, PTB7-Th:IOTIC-2F_a, and PTB7-Th:IOTIC-4F blends exhibit energetic offsets of approximately 0.050, 0.065, and 0.080 eV, respectively.

Next, losses due to recombination, which can be divided into radiative (ΔV_{rad}) and non-radiative losses ($\Delta V_{non-rad}$) are quantified (Equation S4, Supporting Information). As derived from a detailed balance analysis, about 0.200–0.250 eV of radiative recombination is needed to establish thermodynamic equilibrium.^[58] On the other hand, it has been shown that a large part of recombination losses occur non-radiatively, spanning a range of 0.210–0.550 eV.^[59,60] In recent years, there have been numerous reported studies showing correlations between non-radiative recombination losses and carbon-carbon bond vibrations,^[59] molecular orientation at the donor-acceptor interface,^[51,61] energetic driving force,^[3,5,9] and E_{CT} values.^[59]

From the equations described in Section 4.3, Supporting Information, losses due to radiative recombination in the PTB7-Th:IOTIC, PTB7-Th:IOTIC-2F_a, and PTB7-Th:IOTIC-4F blend systems are calculated to be 0.227 ± 0.003 , 0.212 ± 0.003 , and 0.203 ± 0.003 eV, respectively. Inserting the experimentally measured EQE_{EL} (Figure S9, Supporting Information) into Equation S6, the losses due to non-radiative recombination in the PTB7-Th:IOTIC, PTB7-Th:IOTIC-2F_a, and PTB7-Th:IOTIC-4F blend systems are determined to be 0.290 ± 0.003 , 0.305 ± 0.003 , and 0.338 ± 0.003 eV, respectively. The measured non-radiative recombination values are further confirmed by the calculated non-radiative recombination losses, using the procedures described in Section 4.3, Supporting Information. The breakdown of the voltage losses from S_1 to V_{OC} comprising of losses from charge transfer and charge recombination in the three blend systems are summarized in **Table 2** and shown schematically in Figure 3.

In this study, increased non-radiative recombination losses are observed with a concomitant decrease in the radiative recombination losses as the energetic offsets in the blend systems are increased (from PTB7-Th:IOTIC to PTB7-Th:IOTIC-4F). The suppression of non-radiative recombination losses with decreased energetic offset has been observed in several previously reported studies.^[3,5,9,59] This observation can be explained by the idea that a decreased overlap of the vibrational wave function of the CT and ground state leads to the suppression of the non-radiative recombination pathway.^[59] Additionally, the recent paper by Qian et al.^[5] suggests that in low energetic offset systems, hybridization of the CT state with the highly emissive S_1 state will increase the radiative ability of the CT state through the intensity borrowing mechanism.^[62,63] From the modeling of excitonic and CT states, it was found that if the radiative relaxation channel can be made efficient in this way, the non-radiative voltage losses should decrease.^[5] The three blend systems reported here provide a suitable platform, by systematically varying the S_1 -CT offset, to experimentally measure such a trade-off between the radiative and non-radiative recombination losses, for the first time. To further corroborate that the S_1 states of the acceptors are in fact relatively more emissive than the blends, we measured the EQE_{EL} of the acceptor only devices, (Figure S10, Supporting Information), confirming the consistently lower non-radiative recombination values in the acceptor only devices by approximately 0.04 eV [IOTIC ($\Delta V_{non-rad}$) = 0.250 ± 0.003 eV; IOTIC-2F_a ($\Delta V_{non-rad}$) = 0.270 ± 0.003 eV; IOTIC-4F ($\Delta V_{non-rad}$) = 0.300 ± 0.003 eV], compared to that of the blends.

Moreover, to rule out differences in energetic disorder between the blends as a major contributor to the voltage losses, the density of states (DOS) spectra of the three blends were measured by using energy-resolved electrochemical impedance spectroscopy (ER-EIS).^[32,64,65] (Details about the ER-EIS technique and measurements are described in Supporting Information). Figure S11, Supporting Information shows the DOS spectra of the three studied blend systems obtained from ER-EIS, which exhibit no distinct differences suggesting that the energetic disorder in the three blend systems are comparable. Additionally, as a further confirmation of the similarities in the exponential tail states disorder in the three blend systems, the Urbach energies (E_U) from the tail states of highly sensitive EQE spectra of $E_U \approx 25$ meV were determined (details in Figure S12, Supporting Information). An Urbach energy approaching a thermal energy of $E_U \approx kT$ may suggest that the contribution to the voltage losses in the systems from energetic disorder is minimal.^[7,32,57,66,67] It is worth noting that the Urbach energy measurements may lead to some uncertainty in disordered

materials^[68] and cannot be directly comparable to the ER-EIS method, which gives disorder contributions coming from the HOMO and LUMO DOS distributions separately. Nevertheless, from these analyses, the possible effects of differences in the DOS distributions of the three studied blend systems on the charge generation, recombination, and extraction dynamics can be excluded.

2.4. Probing the Charge Generation Dynamics

To investigate the effect of decreasing energetic offsets on the charge generation dynamics of the three blend systems, ultrafast (100 fs–2 ns) transient absorption (TA) spectroscopy were performed. Initially, we conducted TA in both the visible (500–950 nm) and NIR (1050–1300 nm) spectral regions on films of the NFA blended with a non-interacting polymer, polystyrene (PS), to determine the spectral features and exciton lifetimes associated with the acceptor materials. These blend films were fabricated by using an identical polymer weight fraction and deposition conditions to the optimized PTB7-Th:NFA blend in an attempt to best replicate the morphological properties of the active layer used in the actual device.^[5] All IOTIC derivatives exhibit a ground state bleach (GSB) feature that closely matches the absorption spectra of the material, with two distinct vibronic peaks visible (Figure S13a–f, Supporting Information). Additionally, the photo-induced absorption (PIA) band of the first singlet excited state is centered at around 1200 nm in all of the derivatives (Figure S14a–f, Supporting Information). The lifetime of the excited state is relatively short, owing to the narrow band gaps of the acceptors and the effect of the energy gap law on the rate of the non-radiative transitions.^[69] For IOTIC, the half-life ($t_{1/2}$) of the singlet excited state is 45 ps, for IOTIC-2F_a, $t_{1/2} = 30$ ps and for IOTIC-4F, $t_{1/2} = 35$ ps (Figure S13a–f, Supporting Information).

Next, we examine the visible region TA of the PTB7-Th:NFA blends by selectively exciting the NFA component of these films below the bandgap of PTB7-Th to probe solely the hole transfer process. In the PTB7-Th:IOTIC-4F film, excited at 925 nm with a fluence of $0.51 \mu\text{J cm}^{-2}$ (Figure S15a,b, Supporting Information), we initially observe only the IOTIC-4F GSB at 300–400 fs. After 1 ps, the IOTIC-4F GSB begins to decrease in intensity rapidly and a new positive feature spanning 600–750 nm forms. As the spectral position and vibronic features closely match those of PTB7-Th, it is assigned to the GSB of the polymer, consistent with the bleaching of the PTB7-Th ground state transition by the hole transfer process. Interestingly, as the hole transfer progresses, the IOTIC-4F GSB continues to fall rapidly, and there is only a muted growth of the PTB7-Th GSB. This could be caused by one of two things: rapid recombination leading to excited state population loss, or a new PIA band forming under the GSB regions that has the effect of decreasing the apparent GSB intensity. As the blend demonstrates good IQE, we can rule out the former, as this would result in significantly reduced levels of photocurrent generation and a consequently low IQE. Therefore, we assign this PIA underneath the GSB region as belonging to the electron located on IOTIC-4F, as the PIA of the hole on PTB7-Th has widely been reported to lie at around 1150 nm.^[5,70–72] Additionally, we note the presence

of electro-absorption (EA) features at the band edge of the donor and acceptor, consistent with the separation of charges in OPV blends.^[73] Turning to the PTB7-Th:IOTIC-2F_a blend (Figure S15c,d, Supporting Information), excited at 900 nm with a fluence of $0.87 \mu\text{J cm}^{-2}$, we observe very similar photo-physics to the PTB7-Th:IOTIC-4F blend with a relatively slow hole transfer taking place. However, the PTB7-Th:IOTIC blend, excited at 860 nm with a fluence of $0.50 \mu\text{J cm}^{-2}$ (Figure S15e,f, Supporting Information), exhibits markedly different behavior. In this case, there is no obvious formation of the PTB7-Th GSB until timescales of 300–400 ps, as can be seen in the normalized TA spectra (Figure S16a, Supporting Information). By this point, the GSB features have a much weaker intensity than in the other two blends, implying the presence of a much smaller population of holes due to a higher proportion of exciton decay prior to charge transfer.

To gain a better understanding of the hole transfer timescales in the blends, the TA spectra were deconvoluted using a Genetic Algorithm (GA). In all blends, we observe an initial “pre-charge transfer” spectral species, consisting of the NFA GSB only, and a final “post-charge transfer” species, comprised of both the donor and acceptor GSBs and EA features. The IOTIC-4F and IOTIC-2F_a blends can be readily deconvoluted into these two distinct species (Figure S16b–e, Supporting Information), with their relative contributions to the overall TA spectra at each time point providing insight into the kinetics of the hole transfer process. Comparing these fitted kinetics, we can immediately see that this process is faster for the PTB7-Th:IOTIC-4F blend, with hole transfer completed by 50 ps, compared to 160 ps for the PTB7-Th:IOTIC-2F_a blend (Figure 4a). This can be readily explained by the slightly larger driving energy for the hole transfer from the NFA to the donor in this blend. However, it was not possible to satisfactorily deconvolute the TA spectra of the PTB7-Th:IOTIC blend, likely due to the significant spectral overlap of the donor and acceptor GSBs. Nevertheless, we expect the hole transfer in this blend to be the slowest of the three NFA systems as it possesses the smallest energy offset, consistent with the trend observed between IOTIC-4F and IOTIC-2F_a and the significantly lower remaining GSB intensity.

To confirm our hypothesis that there are significantly fewer charges present in the PTB7-Th:IOTIC blend after selective NFA excitation, we turn to the NIR region where we can directly observe the PIA of the holes on PTB7-Th. All films were excited with a pump wavelength of 800 nm for selective NFA excitation and care was taken to use an extremely low fluence to avoid any non-linear recombination processes (PTB7-Th:IOTIC-4F = $0.13 \mu\text{J cm}^{-2}$, PTB7-Th:IOTIC-2F_a = $0.18 \mu\text{J cm}^{-2}$ and PTB7-Th:IOTIC = $0.17 \mu\text{J cm}^{-2}$) (Figure S17a–f, Supporting Information). For all blends, the initial density of excited states (n_0) created on the NFA were roughly equal, $\approx 3\text{--}4 \times 10^{16} \text{ cm}^{-3}$, a value which is highly comparable to the charge carrier densities in these devices operating under 1-sun illumination, as determined via impedance spectroscopy in the following section. Consequently, these measurements are representative of realistic device operating conditions. In all blends, the singlet PIA at 1200 nm decreases in intensity over similar timescales to the hole transfer process previously observed, leaving behind a long-lived PIA at 1175 nm that belongs to the holes

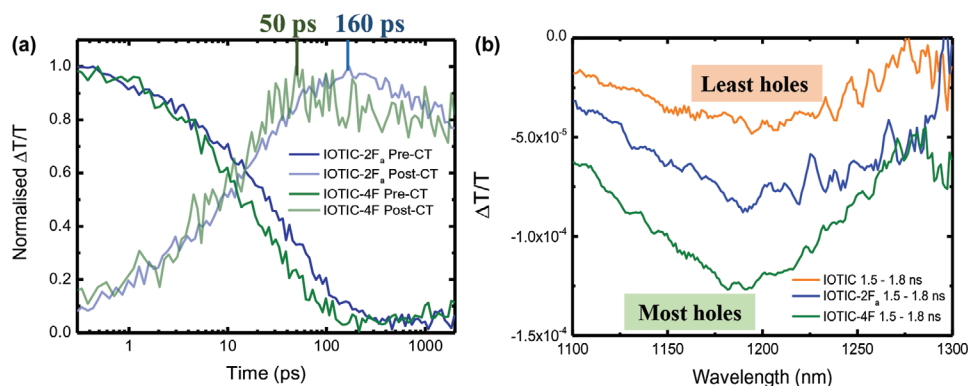


Figure 4. a) Comparison of the hole transfer kinetics for PTB7-Th:IOTIC-2F_a and PTB7-Th:IOTIC-4F blends. b) PIA of the remaining holes on PTB7-Th after hole transfer and exciton decay is completed to gain insight into the relative charge generation efficiencies of the three blend systems.

on PTB7-Th. By comparing the relative intensities of the hole PIA at 1.5–1.8 ns, a timescale where all hole transfer and exciton decay is completed, with only the PIA of the PTB7-Th holes remaining, we can gain insights into the relative charge generation efficiencies of the blends (Figure 4b). We note that the strongest PIA, and therefore the most holes, are found in the PTB7-Th:IOTIC-4F blend, followed by PTB7-Th:IOTIC-2F_a and finally PTB7-Th:IOTIC. This can be rationalized by considering the interplay between exciton decay and hole transfer in the blends: as hole transfer slows with decreasing driving force, it begins to compete with exciton decay. Thus, these processes are finely balanced in low offset NFA OPVs, where even small changes to the rate of one can result in a drastic change in the overall charge generation efficiency.

Additionally, we have also investigated the photophysics of the blend when exciting primarily PTB7-Th with a pump wavelength of 600 nm, a wavelength where there is relatively little absorption by the IOTIC derivatives, but still a quite strong absorption by PTB7-Th. In the visible region, TA of both the PTB7-Th:IOTIC-4F and PTB7-Th:IOTIC-2F_a blends (Figure S18a–d, Supporting Information), the donor and acceptor GSBs are present from the earliest times of 100 fs. This is likely due to some unavoidable direct excitation of the NFA, though the intensity of the NFA GSB suggests other ultrafast processes that lead to bleaching of the NFA ground state have already occurred. However, it is interesting that the PTB7-Th GSB swiftly falls over the first 5 ps (a timescale largely free from hole transfer), whilst the NFA GSB grows in. Following this, the NFA GSB drops rapidly from 5 ps onward, whilst there is a slight growth of the PTB7-Th GSB, consistent with the previously observed timescales of hole transfer. We expect the NFA GSB to drop rapidly when NFA molecules become anionic, due to the presence of the electron PIA under its GSB, as observed when the NFA is selectively excited. However, the growth of this feature over timescales where one might expect electron transfer to occur is a surprise. It suggests that rather than solely electron transfer occurring from PTB7-Th to the NFA, a significant amount of energy transfer is occurring too. This population transfer from donor to acceptor would explain the rise of the NFA GSB and fall of the PTB7-Th GSB on ultrafast timescales. The presence of Förster Resonance Energy Transfer (FRET) is not surprising, given the significant

overlap of the PTB7-Th emission spectrum^[5] with the NFA high oscillator strength absorption and has previously been observed in other NFA systems.^[74] In the IOTIC blend (Figure S18e,f, Supporting Information), it appears that a significant amount of FRET also occurs, but due to the relative inefficiency of the hole transfer process, the GSB of both the donor and acceptor continue to fall rapidly after FRET. The presence of FRET in these blends serves to underline the importance of the balance between the NFA exciton decay and hole transfer rates, as the majority of the charge generation appears to proceed through the lower gap NFA, regardless of on which component the exciton was initially generated. Thus, the trend of decreasing J_{SC} with decreasing offset between the devices can at least partly be explained by differences in hole transfer rates, controlled by the small changes in driving energy.

2.5. Understanding the Non-Geminate Recombination and Charge Extraction Dynamics

To gain further insights on the timescales of the loss processes of the three blend systems, we measured the non-geminate recombination and extraction dynamics. As a guideline, in any OSC device, the goal is to minimize the charge extraction time, while maximizing the charge carrier lifetime, as this leads to a reduction of non-geminate charge recombination.^[6,21,22] To begin this analysis, as a first step, the photocurrent density (J_{ph}) of the devices were calculated.

$$J_{ph} = J_{light} - J_{dark} \quad (2)$$

where J_{light} is the current density under illumination and J_{dark} is the current density in the dark (Figure S19a, Supporting Information). The differences in V_{OC} of the studied blend systems have to be taken into account, which is why the photocurrent density is plotted against the effective voltage ($V_0 - V_{cor}$; where V_0 is the voltage at which $J_{ph} = 0$). Furthermore, the corrected voltage V_{cor} can be obtained by subtracting the voltage losses over the series resistance.

$$V_{cor} = V_{app} - J \cdot R_{series} \quad (3)$$

where J is the current density, and R_{series} is the series resistance which is assumed to be equal to the saturated differential resistance at forward biases (i.e., $\partial V_{\text{app}}/\partial J = \text{constant}$).^[11] When comparing the photocurrents J_{ph} of the three blend systems, a clear trend can be observed, where the values for J_{ph} increase with increasing number of fluorine atoms in the NFA. In addition, it is possible to estimate the probability of charge collection (P_C) by the ratio between the saturated photocurrent density $J_{\text{ph,sat}}$ and the values for J_{ph} at different biases.^[75]

$$P_C = \frac{J_{\text{ph}}}{J_{\text{ph,sat}}} \quad (4)$$

As can be seen in Figure S19b, Supporting Information, the P_C retains comparatively high values for the PTB7-Th:IOTIC-4F blend, while a steeper reduction of P_C can be observed for the other two NFAs at forward biases. In particular, this observation suggests that the PTB7-Th:IOTIC-4F devices exhibit advantageous charge collection, while the PTB7-Th:IOTIC-2F_a and PTB7-Th:IOTIC devices are both afflicted by inferior charge collection.

As was previously established (Section 2.2), all three blend systems exhibited behaviors consistent with $s \approx 1$ kT/q at temperatures down to 200 K, indicating dominant bimolecular recombination processes in the three blends. Nevertheless, an advanced recombination analysis is still needed for a quantitative confirmation of the dominant loss processes.^[76] This can be done based on a quantitative analysis that utilizes capacitance spectroscopy.^[77–79] The capacitance of the BHJ obtained via this measurement technique can be used to determine the charge carrier density (n) and the effective mobility (μ_{eff}) of the studied solar cells under operating conditions (Figure S19c,d, Supporting Information).^[21,80] The details for the procedures used to determine the charge carrier densities and effective mobilities under operating conditions are described in Section 6.1, Supporting Information (Figure S20, Supporting Information). The measured charge carrier densities for these blend systems are in a range of $n = 10^{16}$ – 10^{17} cm^{-3} , with the PTB7-Th:IOTIC-4F blend exhibiting the highest values ($n = 1.2 \times 10^{17}$ cm^{-3}) compared to the PTB7-Th:IOTIC-2F_a ($n = 5.6 \times 10^{16}$ cm^{-3}) and PTB7-Th:IOTIC ($n = 5.8 \times 10^{16}$ cm^{-3}) blends under open-circuit conditions (Figure S19c, Supporting Information). Under reverse bias, the highest carrier density was measured for the PTB7-Th:IOTIC blend ($n = 4.5 \times 10^{16}$ cm^{-3}), which is only slightly lower than the values at open-circuit conditions. This observation could be a sign for inefficient charge extraction, as there should be a significant reduction in the carrier density at reverse biases. In contrast, the PTB7-Th:IOTIC-4F blend shows the lowest carrier density at reverse bias ($n = 2.2 \times 10^{16}$ cm^{-3}), indicating comparatively good extraction, which was also underscored by its high values for the P_C . Moreover, a clear trend can be seen for the effective mobilities, with the PTB7-Th:IOTIC-4F devices having the highest values ($\mu_{\text{eff}} = (2.7\text{--}6.1) \times 10^{-5}$ $\text{cm}^2 \text{V}^{-1} \text{s}^{-1}$), followed by the PTB7-Th:IOTIC-2F_a ($\mu_{\text{eff}} = (1.4\text{--}5.1) \times 10^{-5}$ $\text{cm}^2 \text{V}^{-1} \text{s}^{-1}$), and the PTB7-Th:IOTIC having the smallest effective mobilities ($\mu_{\text{eff}} = (0.7\text{--}5.5) \times 10^{-5}$ $\text{cm}^2 \text{V}^{-1} \text{s}^{-1}$).

Next, a full quantitative analysis approach for the determination of the non-geminate recombination dynamics was adopted

to obtain the bimolecular recombination coefficients (k_{bim}) for the three blend systems (Figure S21, Supporting Information; detailed procedure described Supporting Information). From this analysis, it was found that all three blend systems show, across the entire voltage range, similar k_{bim} values ranging from $(0.18\text{--}2.20) \times 10^{-12}$ $\text{cm}^3 \text{s}^{-1}$. As the bimolecular recombination coefficients between the blends are quite similar, this alone cannot explain the performance differences in the three blend systems. Therefore, the extraction of charge carriers has to also be quantified to obtain a comprehensive understanding of the recombination dynamics in the studied devices. To this end, the effective extraction time (τ_{ex}) was calculated. For this analysis, it was assumed that a charge carrier traverses, on average, half of the active layer thickness, until it reaches one of the electrodes and that the active layer can be treated as an effective medium.^[22] The following relationship can be derived based on these assumptions.

$$\tau_{\text{ex}} = \frac{qLn}{J} \quad (5)$$

where L is the active layer thickness, q is the elementary charge, n is the charge carrier density, and J is the current density obtained from the J - V curves.^[11] A direct comparison of the extraction time (τ_{ex}) and the charge carrier lifetime (τ_{rec}) can be made by rearranging Equation S16, Supporting Information and then be used to assess and understand the relative contributions of the competing non-geminate recombination and extraction processes, as shown in Figure S22, Supporting Information.^[11] In particular, it turns out that the PTB7-Th:IOTIC blend has a significantly slower $\tau_{\text{ex}} = 8.5\text{--}107$ μs over the voltage range examined, compared to the other two blends: PTB7-Th:IOTIC-2F_a ($\tau_{\text{ex}} = 2.3\text{--}54.9$ μs) and PTB7-Th:IOTIC-4F ($\tau_{\text{ex}} = 1.6\text{--}33.2$ μs). Ultimately, the voltage-dependent competition factors, which is defined as the ratio between the recombination and extraction times ($\theta = \tau_{\text{ex}}/\tau_{\text{rec}}$) serves as a metric for understanding the superior FF and J_{SC} values of the PTB7-Th:IOTIC-4F-based devices (Figure 5). The PTB7-Th:IOTIC and PTB7-Th:IOTIC-2F_a devices show similar competition factors ($\theta = 0.003\text{--}10$) over the voltage range investigate, whereas the PTB7-Th:IOTIC-4F devices show significantly smaller competition factors ($\theta = 0.0006\text{--}2$) (Figure 5). Generally, smaller competition factors have been shown to correlate to higher FF and J_{SC} values.^[21,22] As a point of comparison, in our recently published work^[11] on the PM6:Y6 BHJ OSCs with over 15% PCEs, we calculated very low θ values ranging from 0.0002 to 0.56 over the relevant voltage range, due to exceptionally fast charge extraction compared to non-geminate recombination in the blend. Therefore, the low voltage-dependent competition factor in the PTB7-Th:IOTIC-4F devices can be explained by a favorable combination of fast extraction and long charge carrier lifetimes, which is absent in the PTB7-Th:IOTIC and PTB7-Th:IOTIC-2F_a blends.

2.6. Morphological Insights to Understand Device Photophysics

The photophysical phenomena of OSCs are directly linked to its complicated BHJ morphology, which has been shown to

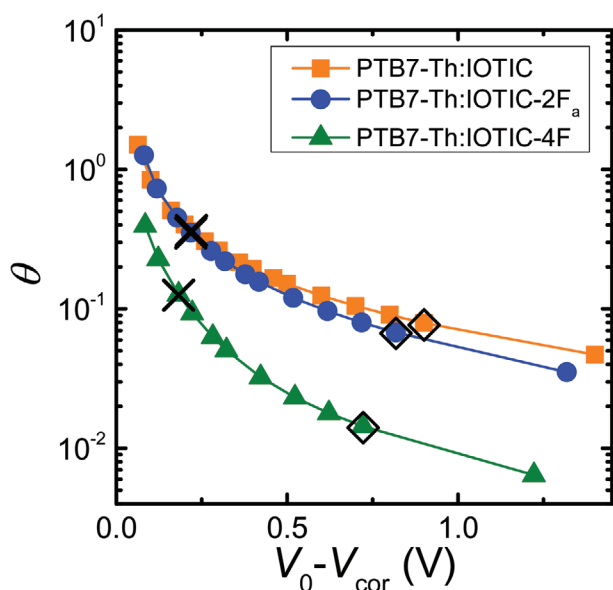


Figure 5. Voltage-dependent competition factor (θ), the ratio between the extraction and recombination times, of the three blend systems. Relevant operating conditions such as maximum power (crosses) and short-circuit (open diamond symbols) conditions are highlighted.

influence the charge generation, recombination, and extraction processes.^[6,11,51,81–84] By analyzing BHJ morphologies over different length scales (from μm to sub-nm) it is possible to evaluate the roles of different structural features on the device photophysics of the blend systems. To begin, photoconductive atomic force microscopy (pc-AFM) was used to determine the height and photocurrent features at the surface of the active layers. To do this, an electrically conductive Pt/Cr tip was used to scan the surface of the active layers of the tested solar cell devices under white light illumination. During the pc-AFM scan, a white light source was focused on the area of scanning, which enabled the photo-responsive features in the blend film to be spatially mapped. A comparison of the photocurrent images normalized to the device with the highest photocurrent (PTB7-Th:IOTIC-4F) across multiple biases (Figure S23, Supporting Information) confirmed that the highest photocurrents are obtained for the PTB7-Th:IOTIC-4F blend, followed by the PTB7-Th:IOTIC-2F_a and PTB7-Th:IOTIC blends. This trend of nanoscale photocurrents is in agreement with what was observed in the J_{SC} of the tested devices (Figure 2) and can be seen in the photocurrent scale readings shown in Figure S24, Supporting Information. However, we were unable to resolve any significant differences in the sizes of the photo-conductive domains of the three blend films with high resolution ($1 \times 1 \mu\text{m}$) pc-AFM (Figure S25, Supporting Information).

Next, we probe the molecular orientation and long-range ordering in the films using GIWAXS. Analyses of GIWAXS (Figures S26 and S27, Supporting Information) on the three blend films mostly showed face-on orientation with significant isotropic scattering making it difficult to unambiguously characterize differences in the blend films (details of GIWAXS analyses are included in the Section 8, Supporting Information). It must be further highlighted here that, while techniques such as pc-AFM and GIWAXS provide useful insights, interpretations

of the overall BHJ morphology using just these techniques can be limiting because they can either only be used to access the surface of the BHJ blend, in the case of pc-AFM, or only the ordered regions of the BHJ film, in the case of GIWAXS. Therefore, we turn to advanced tools, such as RSoXS and solid-state NMR techniques for insights on more nuanced morphological traits, such as the nature of the domain purity and sizes, and the local ordering and interactions of the donor and acceptor species in the blend systems.

The RSoXS technique uses soft X-rays, which are well suited for studying organic blends comprising of carbon or nitrogen atoms, and is commonly used to probe the domain sizes and the donor and acceptor domain purity in BHJ blends.^[85,86] Figure S28, Supporting Information shows the Lorentz corrected and circularly averaged RSoXS profiles of the three studied blend films. Table S5, Supporting Information summarizes the parameters extracted from fitting the RSoXS profiles. The profiles of the PTB7-Th:IOTIC-4F and PTB7-Th:IOTIC-2F_a blends were fitted with two lognormal peaks, whereas the profile of the PTB7-Th:IOTIC blend was fitted with a single lognormal peak, which suggests that there is a multilength scale morphology in the two former and not in the latter case. Comparing the long-period corresponding to the low- q peak in the three blends shows that the PTB7-Th:IOTIC blend has a higher long period of around 97 nm while the PTB7-Th:IOTIC-2F_a and PTB7-Th:IOTIC-4F blends show smaller and similar long periods of 67 and 68 nm, respectively. Additionally, for the PTB7-Th:IOTIC-2F_a and PTB7-Th:IOTIC-4F blends, the fitting identified the presence of smaller domains (reflected by the high q -peaks), which was negligible in the case of the PTB7-Th:IOTIC blend. The root-mean-square (RMS) composition variation (which is monotonically related to the domain purity) of the three blend systems were determined by obtaining the integrated scattering intensities. A higher value for the RMS composition variation indicates larger average purity of the domains in the blends. Interestingly, it was found that the domain purity was highest for the PTB7-Th:IOTIC blend, followed by the PTB7-Th:IOTIC-2F_a and PTB7-Th:IOTIC-4F blends. A high average purity in the blends has been shown to be related to a smaller D:A interfacial area, due to the reduced distributed acceptor molecules in the polymer-rich phase.^[6,53,86,87] In these systems, an increase in the relative volume fraction of small domains and a decrease in the domain purity with increasing J_{SC} values (from PTB7-Th:IOTIC to PTB7-Th:IOTIC-4F blend) suggests that increased charge generation efficiencies may also be partly attributed to an increase in the D:A interfacial area. This implies that in the studied polymer:NFA blends, charge generation efficiencies may not only be dictated by the increased S_1 -CT energetic offsets, but also further influenced by the amount of D:A interfacial area in the BHJ morphology.

To understand the origins of the differences in charge transport and extraction, solid-state NMR was used to probe differences in the local ordering and D:A interactions of the two blend systems showing the biggest differences in charge transport and extraction timescales. These were the PTB7-Th:IOTIC blend, which was afflicted by the slowest charge extraction ($\tau_{\text{ex}} = 8.5\text{--}107 \mu\text{s}$) and transport ($\mu_{\text{eff}} = (0.7\text{--}5.5) \cdot 10^{-5} \text{ cm}^2 \text{ V}^{-1} \text{ s}^{-1}$) and the PTB7-Th:IOTIC-4F blend, which exhibited the fastest charge extraction

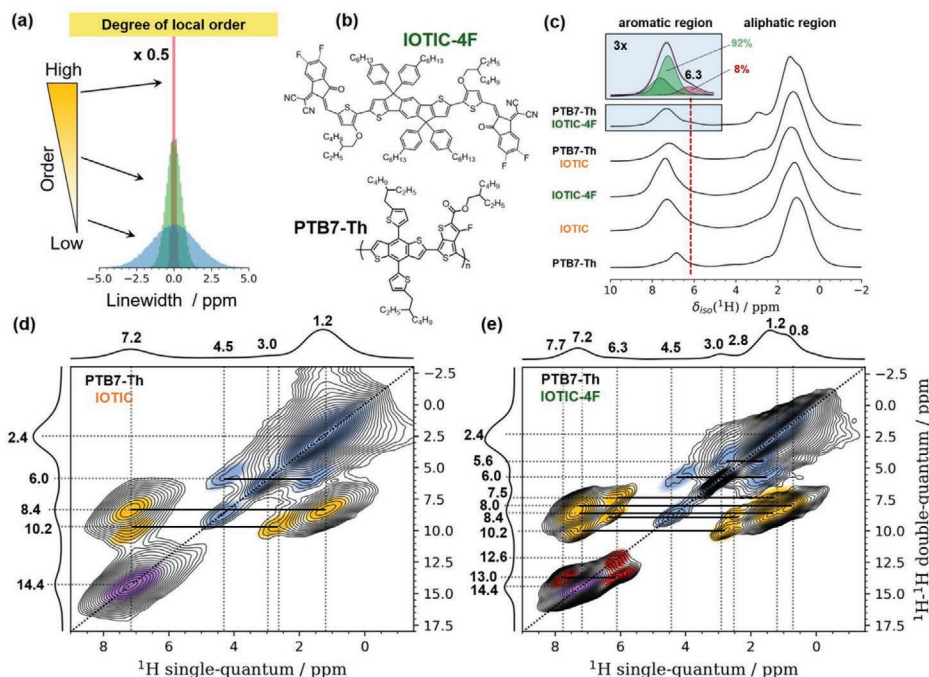


Figure 6. a) Schematic representation of how local order and disorder are manifested in ^1H NMR line shapes. b) Molecular structure of PTB7-Th and IOTIC-4F. c) ^1H MAS NMR spectra of PTB7-Th, IOTIC, IOTIC-4F, and their respective blends acquired at 18.8 T (800 MHz for ^1H) and 28.490 kHz MAS, using a Hahn-Echo to remove the background signal of the probe head. d, e) 2D ^1H - ^1H double-quantum/single-quantum (DQ-SQ) correlation spectra of d) PTB7-Th:IOTIC and e) PTB7-Th:IOTIC-4F acquired using back-to-back DQ-excitation over two rotor periods. Note the difference in linewidths in the 2D spectra. Violet contour-levels indicate intensity correlations between aromatic-aromatic protons, yellow aromatic-aliphatic protons, and blue aliphatic-aliphatic protons. Red contour-levels correspond to intensity correlations between aromatic-aromatic protons associated with the signal at 6.3 ppm. Correlated signals involving these moieties are connected by black bars.

($\tau_{\text{ex}} = 1.6\text{--}33.2 \mu\text{s}$) and transport ($\mu_{\text{eff}} = (2.7\text{--}6.1) \cdot 10^{-5} \text{ cm}^2 \text{ V}^{-1} \text{ s}^{-1}$). Solid-state NMR is sensitive to the local environments of nuclear spins, making it particularly useful to investigate both ordered and disordered materials on a molecular level, which is generally not possible with X-ray diffraction methods. However, characterizing heterogeneous materials containing multiple ordered and disordered domains poses additional challenges, as the NMR signals from the different domains tend to interfere and overlap, resulting in broad spectra that are challenging to resolve and analyze. In the case of polymers, statistical distributions of the local environments of otherwise chemically equivalent nuclei (e.g., ^1H atoms in polymer backbones that experience variations in local π - π packing) are often manifested as broad chemical shift distributions (compare Figure 6a). Similarly, the abundance of near-equivalent species results in large distributions of overlapping signals (e.g., a large number of CH_2 groups in the aliphatic region). A third contribution arises from the anisotropic bulk magnetic susceptibility (ABMS), which is the tendency of a sample to become magnetized in the presence of an external magnetic field. While magic angle spinning (MAS) reduces the influence of the ABMS significantly, it cannot completely remove it, and a small contribution to the observed chemical shift often remains, leading to additional broadening of the resonance.^[88–91] Combined, these effects result in signals with broad, Gaussian line shapes, an effect that is often called “inhomogeneous broadening.”

In addition to the statistical broadening, strong anisotropic spin-spin interactions in the solid-state lead to reduced

coherence lifetimes and thereby increased natural linewidth (exponential broadening, Lorentzian line shapes, also referred to as “homogeneous broadening”). The strength of the anisotropic interactions and thus the extent of lifetime broadening is related to the abundance of the nuclei in question, with ^1H being affected most due to its ubiquity in organic materials and almost 100% natural abundance.

By combining careful data processing and analysis with information gained from powerful 2D, dipolar-mediated correlation NMR spectroscopy techniques, valuable information on the local order and disorder in the polymer:NFA blends can be obtained. Figure 6b,c show schematic diagrams of the molecular structures and ^1H MAS NMR spectra of PTB7-Th, IOTIC, IOTIC-4F, and their respective blends acquired at 800 MHz (18.8 T) at 28.490 kHz MAS and ambient conditions. Two groups of ^1H signals can be discerned, corresponding to signals in the region from 5.5 ppm to 8.0 ppm from aromatic ^1H atoms, and signals in the range of 0 ppm to 3.5 ppm from aliphatic sidechains. The aliphatic protons nearest to the linker groups can be discerned as small, broad peaks in the range of 3–5 ppm. In general, the ^1H MAS NMR spectra are characterized by broad signals with Gaussian-Lorentzian line shapes, indicating a significant distribution of the chemical shifts (Gaussian component), in addition to the broadening caused by the rapid signal decay (Lorentzian component), due to the strong anisotropic spin-spin interactions. The effect of overlapping chemical shifts is exemplified by the aliphatic peak in PTB7-Th, which is a superposition of numerous Lorentzian

lines with slightly different chemical shifts arising from the more than 50 aliphatic ^1H atoms of each monomer. By contrast, the broadening in the aromatic region of the ^1H MAS NMR spectrum of PTB7-Th, which has only three inequivalent ^1H sites on the backbone, is caused by the variation of the chemical shift due to local disorder. The broad component of the aromatic region is assigned to the two protons of the thiophene side group, whereas the narrower signal is assigned to the benzodithiophene unit. The broad line of the former is most likely due to conformational disorder, leading to a Gaussian distribution of chemical shifts.

With the exception of pure PTB7-Th, with its three inequivalent aromatic proton sites per monomer, the aromatic region between 6 and 8 ppm shows few resolved features due to the signal overlap of the numerous aromatic proton sites, though a small, broad shoulder around 6.3 ppm is discernible in the case of the PTB7-Th:IOTIC-4F blend. This signal is not present in either PTB7-Th or IOTIC-4F, indicating that the displaced signal is a result of the blending. Furthermore, a similar shift is not observed for the blend with IOTIC. Displacements of the aromatic ^1H signals to lower ppm values in conjugated polymers is usually a sign of increased ring-current effects caused by neighboring aromatic systems and is commonly associated with strong π - π interactions.^[23,36,92,93] Therefore, the presence of this new signal at 6.3 ppm hints at increased π -packing in the PTB7-Th:IOTIC-4F blend, though whether this occurs in the polymer, the NFA, or at the interface between the two is not discernible, based on the 1D ^1H MAS spectra alone. Interestingly, the ^1H MAS spectrum of the PTB7-Th:IOTIC-4F blend exhibits overall narrower signals with better resolution, especially in the aliphatic range between 0 ppm and 4 ppm.

The aggregation of PTB7-Th, IOTIC, and IOTIC-4F molecules and their interactions in blends can be further assessed by determining their intermolecular proximities, as evidenced by dipole-dipole-coupled species. Powerful 2D ^1H - ^1H double-quantum single-quantum correlation analyses (Figure 6d,e) probe the combined chemical shifts of spin-pairs (double quantum coherences) that are correlated via “through-space” dipolar interactions to the chemical shifts of the respective types of spins (single quantum coherences). These allow correlated signals from pairs of dipole-dipole coupled ^1H nuclei to be resolved and identified in a 2D frequency map, which is typically presented as 2D contour-plot spectrum.^[37,94-96] The excitation efficiency for the double-quantum coherences is directly related to the dipolar coupling strength, which in turn is proportional to the inverse cube of the separation distance, as well as to the DQ-excitation time measured in rotational periods, making this experiment particularly sensitive to ^1H pairs in close spatial proximity (up to 5 Å). In addition, since the chemical shift in the double-quantum dimension (vertical axis) is the sum of the single quantum chemical shifts (horizontal axis), the experiments allow for spin pairs formed by equivalent (“self-correlated” signals, observed along the double diagonal) or inequivalent (“cross-correlated” signals, observed as two peaks with the same double-quantum frequency but with different single-quantum frequencies) to be resolved. Similar to the ^1H MAS NMR spectra, the DQ-SQ spectrum of PTB7-Th:IOTIC shows mostly broad signals with few discernible features, while the spectrum of PTB7-Th:IOTIC-4F exhibits better

resolution, especially in the aromatic region. Both of the spectra show intense self-correlation signals in the aliphatic range of $\delta(^1\text{H})^{\text{SQ}} = 0\text{--}3$ ppm and $\delta(^1\text{H})^{\text{DQ}} = 0\text{--}6$ ppm, the aromatic range $\delta(^1\text{H})^{\text{SQ}} = 6\text{--}8$ ppm, and $\delta(^1\text{H})^{\text{DQ}} = 12\text{--}16$ ppm, as well as cross-correlations between the two regions. The aforementioned signal at around $\delta(^1\text{H})^{\text{SQ}} = 6.3$ ppm is readily observed as cross-correlated to both an aromatic signal at approximately $\delta(^1\text{H})^{\text{SQ}} = 7.7$ ppm and to signals in the aliphatic region. The two cross-correlated signals are observable after just a single rotor period of DQ-excitation, indicating a spatial proximity of 4 Å or less. A weak self-correlated signal at $\delta(^1\text{H})^{\text{SQ}} = 6.3$ ppm and $\delta(^1\text{H})^{\text{DQ}} = 12.6$ ppm becomes apparent at longer recoupling times of two and more clearly after four rotor periods of DQ-excitation (data shown in Supporting Information). Information on the signal at $\delta(^1\text{H})^{\text{SQ}} = 7.7$ ppm is obscured by the overlapping signals in the aromatic region. Overall, the new signal observed at 6.3 ppm is more clearly resolved in the 2D DQ-SQ NMR and data for the blend PTB7-Th:IOTIC-4F shows much better resolution compared to PTB7-Th:IOTIC.

In principle, this can be attributed to two effects, either an increase in local order and thereby a reduction of the width of the chemical shift distribution (less inhomogeneous broadening), or the presence of increased motional averaging leading to longer signal lifetime and narrower lines (less homogeneous broadening).^[94,97-99] To distinguish between the two cases, we performed ^1H - ^{13}C DIPSHIFT experiments on both blends.^[100-102] The objective of the experiment was to quantify the degree of motional averaging by measuring the apparent strength of the ^1H - ^{13}C dipolar couplings of CH or CH_2 moieties and comparing these to theoretical values.^[101,103] Details of the experiment are provided in the Supporting Information; data obtained for both blends show no significant differences in the extents of motional averaging between the two. Thus, the narrower ^1H NMR signals in the PTB7-Th:IOTIC-4F blend are most likely the result of decreased inhomogeneous broadening, indicating a higher extent of atomic-level order in PTB7-Th:IOTIC-4F, compared to PTB7-Th:IOTIC.

The presence of a single, relatively isolated fluorine moiety in the polymer backbone of PTB7-Th offers the potential to probe the molecular-level environment of the donor polymer backbone through ^{19}F MAS NMR. In a similar fashion, the fluorine atom of the acceptor material IOTIC-4F enables the molecular-level environment of the NFA also to be established. 1D ^{19}F MAS NMR spectra of PTB7-Th, IOTIC-4F, and the two blends PTB7-Th:IOTIC-4F and PTB7-Th:IOTIC were acquired and are shown in Figure 7a. The spectrum of PTB7-Th shows a broad, predominantly Gaussian signal at -111 ppm with a full-width-at-half-maximum, FWHM of $\Delta\delta(^{19}\text{F}) = 6.2$ ppm. Furthermore, apart from a reduction in the intensity of this signal due to the dilution, the signal appears unchanged in the two blends. The large ^{19}F width and Gaussian line shape associated with the fluorine atoms in PTB7-Th are indicative of a significant degree of local disorder of the polymer backbone, though whether this is related to conformational or π -packing disorder is unclear. ABMS effects might also contribute to the linewidth, though those reported in literature are usually smaller (below 2 ppm in diamagnetic samples, often 1 ppm or less).^[89,90] The effect of the bulk magnetic susceptibility is expected to affect all of the signals equally, leading to similar broadening of the

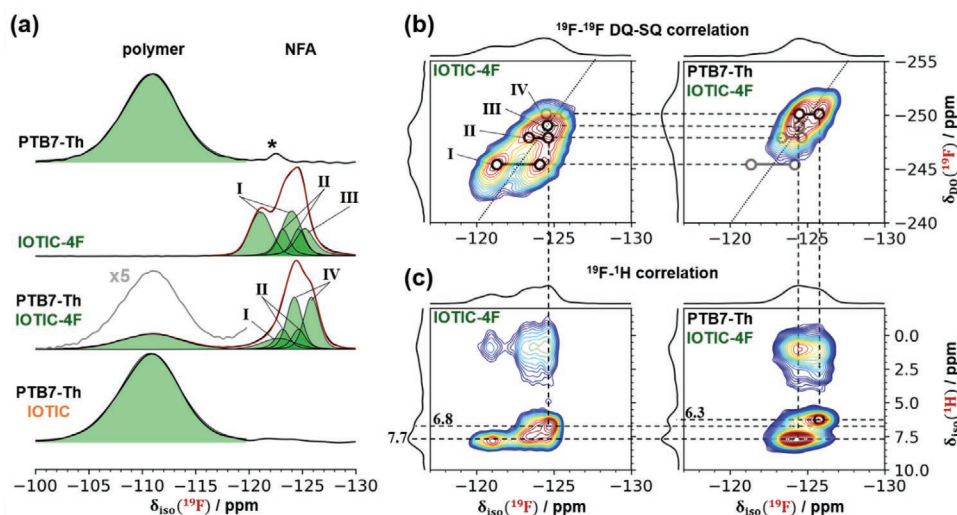


Figure 7. a) 1D ^{19}F MAS NMR spectra of PTB7-Th, IOTIC-4F, PTB7-Th:IOTIC-4F, and PTB7-Th:IOTIC, acquired at 9.4 T and 25.0 kHz MAS. Deconvoluted signals are shown in green; the asterisk marks a small PTFE impurity. The Roman numerals denote ^{19}F signals from dipole–dipole-coupled moieties, as determined from b) 2D ^{19}F - ^{19}F double-quantum/single-quantum (DQ-SQ) correlation spectra. c) 2D ^{19}F - ^1H heteronuclear correlation spectra of the pure NFA IOTIC-4F and its blend with PTB7-Th. Only the shift ranges corresponding to the NFA are shown.

^1H , ^{19}F and ^{13}C signals in a given domain when measured in units relative to the Larmor frequency (ppm).

Compared to the broad ^{19}F signal associated with the polymer backbone, the ^{19}F signals from the fluorine moieties in IOTIC-4F are much narrower ($\Delta\delta(^{19}\text{F}) = 1.5\text{--}2$ ppm, FWHM), though several overlapping signals are observed for neat IOTIC-4F as well as in the blend. Differences in the isotropic ^{19}F chemical shift are most likely linked to polymorphism of the IOTIC-4F in the two blends, or the presence of commingled crystalline and amorphous fractions. The much narrower, more Lorentzian-shaped ^{19}F lines of IOTIC-4F indicate a higher degree of local order in the NFA part of the PTB7-Th:IOTIC-4F blend. 2D ^{19}F - ^{19}F double-quantum single-quantum 2D correlation and ^{19}F - ^1H heteronuclear-correlation NMR spectra (Figure 7b,c) provide the resolution necessary to distinguish the overlapping signals. These reveal a number of correlated signals (indicated by Roman numerals in Figure 7), with signal labels I, II, and III being observed in the case of neat IOTIC-4F, and a new set of signals IV dominating the 2D ^{19}F - ^{19}F NMR spectrum of the blend. These groups of signals in the 2D ^{19}F - ^{19}F data correspond to different pairs of fluorine atoms in individual IOTIC-4F molecules, which in turn are in different molecular environments (i.e., different polymorphs or commingled fractions). The observation of a new group (IV) indicates the blending with PTB7-Th leads to significant changes in the molecular level environment of the NFA.

Further, 2D ^{19}F - ^1H heteronuclear correlation spectra in Figure 7c show correlated intensity between the ^{19}F signal at -126 ppm associated with group IV, and the ^1H signal at 6.3 ppm, indicating that the increased π - π interactions previously associated with this ^1H signal are occurring either in the NFA or at the polymer:NFA interface. Therefore, solid-state NMR analyses indicate that the superior charge transport and extraction properties in the PTB7-Th:IOTIC-4F blend can be explained by the increased atomic-level local ordering and π - π interactions in present in the blend.

2.7. Effects of Changing the NFA Chemical Structure on Charge Generation, Recombination, Extraction, and Voltage Losses that Dictate PCEs

In the studied polymer:NFA systems, we found that upon changing the chemical structures of the NFAs via fluorination, we were inevitably changing two major things that affected the device performance: energetic offsets and device morphology. The objective of this study was to systematically deconvolute the impact of changing both energetic offsets and morphology on the device performance. First, to see the effect of changing energetic offsets on the device parameters, charge generation dynamics at the D:A interface and voltage losses were measured. Transient absorption spectroscopy was used to measure the charge generation dynamics, where it was found that hole transfer slows with decreasing energetic driving force, which can lower the J_{SC} generated from the devices. A systematic study achieved by affirming that bimolecular recombination is the dominant pathway in all blend systems, and losses due to energetic disorder as well as trap-assisted recombination were minimal, helped identify and accurately compare origins of the radiative and non-radiative recombination losses. More specifically, we found that the increase in the V_{OC} was due to a decrease in the non-radiative recombination losses as energetic offsets were decreased due to the intensity borrowing mechanism and the design rules formulated in a previous study.^[5] Second, an in-depth study of the thin-film morphology (i.e., D:A interfacial area, local ordering, and π - π interactions) in the blend systems obtained from RSoXS and solid-state NMR spectroscopy analyses led us to understand why the highest performing devices exhibit the most superior FF and J_{SC} values. Specifically, we found that increased D:A interfacial area obtained from RSoXS measurements in the blends can be correlated to increased charge generation efficiencies, which further contributed to higher J_{SC} values. Additionally, increased local ordering and π - π interactions were characterized by

solid-state NMR spectroscopy in the PTB7-Th:IOTIC-4F blend. Since the increase in local ordering and π - π interactions are present in the PTB7-Th:IOTIC-4F blend, but absent in the PTB7-Th:IOTIC blend, the apparent increase should be linked to fluorination. These changes in the local ordering and π - π interactions have led to the fastest charge transport and the best competition factors ($\tau_{\text{ex}} \ll \tau_{\text{rec}}$) resulting in the highest FF and J_{SC} values in the PTB7-Th:IOTIC-4F blend.

3. Conclusions

In summary, this work builds upon recent novel findings on the device photophysics of polymer:NFA blends starting from early timescales of photoexcitation to longer timescales of charge extraction at the electrodes. Specifically, a deconvolution of the different loss processes in polymer:NFA blends and the connections to nuanced BHJ morphology and energetics were established in a systematic study. Whilst this study is limited to these three polymer:NFA blends, these results are representative of a more general trend of the effect of fluorination on OPV properties. This is because fluorination is likely to induce similar changes in the blend properties, regardless of the parent class of NFA.^[5,25,26,28–30] Furthermore, the detailed findings of the impact of bulk and interfacial morphology on device performance can be more widely applicable to many NFA systems. The primary conclusions from this work are as follows.

- I) We were able experimentally measure a tradeoff between the radiative and non-radiative recombination losses by systematically varying the S_1 -CT offsets, by fluorinating a series of NFAs. For a systematic comparison of the total voltage losses between the three systems, we established that all three blend systems showed dominant bimolecular recombination loss processes at temperatures down to 200 K, and that losses due to energetic disorder were comparable and minimal in all three systems.
- II) Insights into the relative charge generation efficiencies of the three blends showed that as hole transfer slows with decreasing energetic driving force, it begins to compete with exciton decay. Furthermore, the presence of FRET in these blends underlines the importance of the balance between the NFA exciton decay and hole transfer rates, as the majority of the charge generation appears to proceed through the lower gap NFA, regardless of on which component the exciton was initially generated. Therefore, it was found that these processes are finely balanced in low energetic offset polymer:NFA blends, where small changes to hole transfer rates can notably deteriorate the charge generation efficiencies and ultimately the current generated from the devices.
- III) In the studied polymer:NFA blends, the competition between non-geminate recombination and extraction dynamics in the three blend systems were shown to correlate with the FF and J_{SC} values. Superior FF and J_{SC} values in the PTB7-Th:IOTIC-4F blend were found to be due to a favorable combination of slow recombination and fast extraction dynamics leading to smaller competition factors and enhanced charge transport. RSoXS data suggests that an increased D:A interfacial area with increasing energetic

offsets may further aid in the charge generation efficiencies of the studied polymer:NFA blend systems. Solid-state NMR provides detailed atomic-level insights on the nature and origins of the increased local ordering and π - π interactions in the NFA or at the polymer:NFA interface, which explain the superior charge transport and extraction in the PTB7-Th:IOTIC-4F devices.

Ultimately, the enhanced J_{SC} and FF values in the highest performing blend system (PTB7-Th:IOTIC-4F), as a result of a beneficial atomic-level local ordering (which affects charge transport and extraction) and a favorable S_1 -CT offset and D:A interfacial area (which affects charge generation), were found to outweigh the increased voltage losses, to yield the highest PCEs. Comprehensive studies of this nature, which focus on ascertaining the fundamental mechanisms and processes by which high power conversion efficiencies are achieved, can increase the likelihood of achieving even higher efficiencies, bringing us a step closer to the commercialization of OSCs in the near future.

Supporting Information

Supporting Information is available from the Wiley Online Library or from the author.

Acknowledgements

A.K., J.V., A.J.G., and P.S. contributed equally to this work. This work was supported by the Department of the Navy, Office of Naval Research Award No. N00014-14-1-0580. A.K. acknowledges funding by the Schlumberger foundation. J.V. acknowledges funding by the Alexander-von-Humboldt Stiftung. This research used resources of the Advanced Light Source, which is a DOE Office of Science User Facility under contract no. DE-AC02-05CH11231. The solid-state NMR experiments were carried out in the Shared Facilities of the UCSB Materials Research Laboratory, supported by the MRSEC Program of the NSF under Award DMR—170256, which is a member of the NSF-funded Materials Research Facilities Network (www.mrfln.org). Z.P. and H.A. were supported by the U.S. Office of Naval Research (ONR), under Award No. N000141712204. V.N. would like to acknowledge VEGA under the project number 2/0081/18 and the Center for Advanced Material Application, SAS. R.H.F. and A.J.G. acknowledge support from the Simons Foundation (grant no. 601946). The authors would like to thank Dr. Alexander A. Mikhailovsky, Dr. Viktor Brus, Dr. Seo-Jin Ko, Katie D. Rosenthal, and Benjamin R. Luginbuhl for helpful discussions.

Conflict of Interest

The authors declare no conflict of interest.

Keywords

charge extraction, charge generation, charge recombination, non-fullerene acceptors, resonant soft X-ray scattering, solid-state NMR, voltage losses

Received: April 6, 2020

Revised: June 5, 2020

Published online: June 18, 2020

- [1] Q. Liu, Y. Jiang, K. Jin, J. Qin, J. Xu, W. Li, J. Xiong, J. Liu, Z. Xiao, K. Sun, S. Yang, X. Zhang, L. Ding, *Sci. Bull.* **2020**, *65*, 272.
- [2] S. Chen, Y. Wang, L. Zhang, J. Zhao, Y. Chen, D. Zhu, H. Yao, G. Zhang, W. Ma, R. H. Friend, P. C. Y. Chow, F. Gao, H. Yan, *Adv. Mater.* **2018**, *30*, 1804215.
- [3] J. Liu, S. Chen, D. Qian, B. Gautam, G. Yang, J. Zhao, J. Bergqvist, F. Zhang, W. Ma, H. Ade, O. Inganäs, K. Gundogdu, F. Gao, H. Yan, *Nat. Energy* **2016**, *1*, 16089.
- [4] J. Hou, O. Inganäs, R. H. Friend, F. Gao, *Nat. Mater.* **2018**, *17*, 119.
- [5] D. Qian, Z. Zheng, H. Yao, W. Tress, T. R. Hopper, S. Chen, S. Li, J. Liu, S. Chen, J. Zhang, X.-K. Liu, B. Gao, L. Ouyang, Y. Jin, G. Pozina, I. A. Buyanova, W. M. Chen, O. Inganäs, V. Coropceanu, J.-L. Bredas, H. Yan, J. Hou, F. Zhang, A. A. Bakulin, F. Gao, *Nat. Mater.* **2018**, *17*, 703.
- [6] N. A. Ran, J. A. Love, M. C. Heiber, X. Jiao, M. P. Hughes, A. Karki, M. Wang, V. V. Brus, H. Wang, D. Neher, H. Ade, G. C. Bazan, T.-Q. Nguyen, *Adv. Energy Mater.* **2018**, *8*, 1701073.
- [7] N. A. Ran, J. A. Love, C. J. Takacs, A. Sadhanala, J. K. Beavers, S. D. Collins, Y. Huang, M. Wang, R. H. Friend, G. C. Bazan, T.-Q. Nguyen, *Adv. Mater.* **2016**, *28*, 1482.
- [8] K. Kawashima, Y. Tamai, H. Ohkita, I. Osaka, K. Takimiya, *Nat. Commun.* **2015**, *6*, 10085.
- [9] F. D. Eisner, M. Azzouzi, Z. Fei, X. Hou, T. D. Anthopoulos, T. J. S. Dennis, M. Heeney, J. Nelson, *J. Am. Chem. Soc.* **2019**, *141*, 6362.
- [10] Y. Cui, H. Yao, J. Zhang, K. Xian, T. Zhang, L. Hong, Y. Wang, Y. Xu, K. Ma, C. An, C. He, Z. Wei, F. Gao, J. Hou, *Adv. Mater.* **2020**, *32*, 1908205.
- [11] A. Karki, J. Vollbrecht, A. L. Dixon, N. Schopp, M. Schrock, G. N. M. Reddy, T.-Q. Nguyen, *Adv. Mater.* **2019**, *31*, 1903868.
- [12] B. Fan, D. Zhang, M. Li, W. Zhong, Z. Zeng, L. Ying, F. Huang, Y. Cao, *Sci. China: Chem.* **2019**, *62*, 746.
- [13] Y. Cui, H. Yao, J. Zhang, T. Zhang, Y. Wang, L. Hong, K. Xian, B. Xu, S. Zhang, J. Peng, Z. Wei, F. Gao, J. Hou, *Nat. Commun.* **2019**, *10*, 2515.
- [14] D. Baran, T. Kirchartz, S. Wheeler, S. Dimitrov, M. Abdelsamie, J. Gorman, R. S. Ashraf, S. Holliday, A. Wadsworth, N. Gasparini, P. Kaienburg, H. Yan, A. Amassian, C. J. Brabec, J. R. Durrant, I. McCulloch, *Energy Environ. Sci.* **2016**, *9*, 3783.
- [15] W. Zhao, D. Qian, S. Zhang, S. Li, O. Inganäs, F. Gao, J. Hou, *Adv. Mater.* **2016**, *28*, 4734.
- [16] D. Baran, N. Gasparini, A. Wadsworth, C. H. Tan, N. Wehbe, X. Song, Z. Hamid, W. Zhang, M. Neophytou, T. Kirchartz, C. J. Brabec, J. R. Durrant, I. McCulloch, *Nat. Commun.* **2018**, *9*, 2059.
- [17] C.-H. Tan, J. Gorman, A. Wadsworth, S. Holliday, S. Subramaniyan, S. A. Jenekhe, D. Baran, I. McCulloch, J. R. Durrant, *Chem. Commun.* **2018**, *54*, 2966.
- [18] L. Perdigón-Toro, H. Zhang, A. Markina, J. Yuan, S. M. Hosseini, C. M. Wolff, G. Zuo, M. Stolterfoht, Y. Zou, F. Gao, D. Andrienko, S. Shoaee, D. Neher, *Adv. Mater.* **2020**, *32*, 1906763.
- [19] C. Göhler, A. Wagenpfahl, C. Deibel, *Adv. Electron. Mater.* **2018**, *4*, 1700505.
- [20] H. Cha, S. Wheeler, S. Holliday, S. D. Dimitrov, A. Wadsworth, H. H. Lee, D. Baran, I. McCulloch, J. R. Durrant, *Adv. Funct. Mater.* **2018**, *28*, 1704389.
- [21] M. C. Heiber, T. Okubo, S.-J. Ko, B. R. Luginbuhl, N. A. Ran, M. Wang, H. Wang, M. A. Uddin, H. Y. Woo, G. C. Bazan, T.-Q. Nguyen, *Energy Environ. Sci.* **2018**, *11*, 3019.
- [22] D. Bartesaghi, I. delC. Pérez, J. Kniepert, S. Roland, M. Turbiez, D. Neher, L. J. A. Koster, *Nat. Commun.* **2015**, *6*, 7083.
- [23] P. Selter, M. R. Hansen, in *NMR Methods for Characterization of Synthetic and Natural Polymers*, (Eds: R. Zhang, T. Miyoshi, P. Sun), Royal Society of Chemistry, London, UK **2019**, Ch.16, pp. 363–386.
- [24] L. Ye, H. Hu, M. Ghasemi, T. Wang, B. A. Collins, J.-H. Kim, K. Jiang, J. H. Carpenter, H. Li, Z. Li, T. McAfee, J. Zhao, X. Chen, J. L. Y. Lai, T. Ma, J.-L. Bredas, H. Yan, H. Ade, *Nat. Mater.* **2018**, *17*, 253.
- [25] J. Sun, X. Ma, Z. Zhang, J. Yu, J. Zhou, X. Yin, L. Yang, R. Geng, R. Zhu, F. Zhang, W. Tang, *Adv. Mater.* **2018**, *30*, 1707150.
- [26] Q. He, M. Shahid, X. Jiao, E. Gann, F. D. Eisner, T. Wu, Z. Fei, T. D. Anthopoulos, C. R. McNeill, M. Heeney, *ACS Appl. Mater. Interfaces* **2020**, *12*, 9555.
- [27] X. Zhang, D. Zhang, Q. Zhou, R. Wang, J. Zhou, J. Wang, H. Zhou, Y. Zhang, *Nano Energy* **2019**, *56*, 494.
- [28] B. Kan, J. Zhang, F. Liu, X. Wan, C. Li, X. Ke, Y. Wang, H. Feng, Y. Zhang, G. Long, R. H. Friend, A. A. Bakulin, Y. Chen, *Adv. Mater.* **2018**, *30*, 1704904.
- [29] S. Dai, F. Zhao, Q. Zhang, T.-K. Lau, T. Li, K. Liu, Q. Ling, C. Wang, X. Lu, W. You, X. Zhan, *J. Am. Chem. Soc.* **2017**, *139*, 1336.
- [30] H. Yao, Y. Cui, R. Yu, B. Gao, H. Zhang, J. Hou, *Angew. Chem., Int. Ed.* **2017**, *56*, 3045.
- [31] K. R. Graham, C. Cabanetos, J. P. Jahnke, M. N. Idso, A. El Labban, G. O. Ngongang Ndjawa, T. Heumueller, K. Vandewal, A. Salleo, B. F. Chmelka, A. Amassian, P. M. Beaujuge, M. D. McGehee, *J. Am. Chem. Soc.* **2014**, *136*, 9608.
- [32] A. Karki, G.-J. A. H. Wetzelaer, G. N. M. Reddy, V. Nádaždy, M. Seifrid, F. Schauer, G. C. Bazan, B. F. Chmelka, P. W. M. Blom, T.-Q. Nguyen, *Adv. Funct. Mater.* **2019**, *29*, 1901109.
- [33] B. Yurash, D. Leifert, G. N. M. Reddy, D. X. Cao, S. Biberger, V. V. Brus, M. Seifrid, P. J. Santiago, A. Köhler, B. F. Chmelka, G. C. Bazan, T.-Q. Nguyen, *Chem. Mater.* **2019**, *31*, 6715.
- [34] M. T. Seifrid, G. N. M. Reddy, C. Zhou, B. F. Chmelka, G. C. Bazan, *J. Am. Chem. Soc.* **2019**, *141*, 5078.
- [35] C. K. Lo, B. R. Gautam, P. Selter, Z. Zheng, S. D. Oosterhout, I. Constantinou, R. Knitsch, R. M. W. Wolfe, X. Yi, J.-L. Bredas, F. So, M. F. Toney, V. Coropceanu, M. R. Hansen, K. Gundogdu, J. R. Reynolds, *Chem. Mater.* **2018**, *30*, 2995.
- [36] A. Melnyk, M. J. N. Junk, M. D. McGehee, B. F. Chmelka, M. R. Hansen, D. Andrienko, *J. Phys. Chem. Lett.* **2017**, *8*, 4155.
- [37] D. Dudenko, A. Kiersnowski, J. Shu, W. Pisula, D. Sebastiani, H. W. Spiess, M. R. Hansen, *Angew. Chem., Int. Ed.* **2012**, *51*, 11068.
- [38] Y. Chang, T.-K. Lau, P. C. Y. Chow, N. Wu, D. Su, W. Zhang, H. Meng, C. Ma, T. Liu, K. Li, X. Zou, K. Sing Wong, X. Lu, H. Yan, C. Zhan, *J. Mater. Chem. A* **2020**, *8*, 3676.
- [39] Z. Fei, P. Boufflet, S. Wood, J. Wade, J. Moriarty, E. Gann, E. L. Ratcliff, C. R. McNeill, H. Sirringhaus, J.-S. Kim, M. Heeney, *J. Am. Chem. Soc.* **2015**, *137*, 6866.
- [40] J. Liu, L.-K. Ma, H. Lin, L. Zhang, Z. Li, W. K. Law, A. Shang, H. Hu, W. Ma, H. Yan, *Small Methods* **2018**, *2*, 1700415.
- [41] T. Kharandiuk, E. J. Hussien, J. Cameron, R. Petrina, N. J. Findlay, R. Naumov, W. T. Klooster, S. J. Coles, Q. Ai, S. Goodlett, C. Risko, P. J. Skabara, *Chem. Mater.* **2019**, *31*, 7070.
- [42] H. Yao, Y. Chen, Y. Qin, R. Yu, Y. Cui, B. Yang, S. Li, K. Zhang, J. Hou, *Adv. Mater.* **2016**, *28*, 8283.
- [43] J. Lee, S. Ko, M. Seifrid, H. Lee, C. McDowell, B. R. Luginbuhl, A. Karki, K. Cho, T. Nguyen, G. C. Bazan, *Adv. Energy Mater.* **2018**, *8*, 1801209.
- [44] G. F. Burkhard, E. T. Hoke, M. D. McGehee, *Adv. Mater.* **2010**, *22*, 3293.
- [45] L. J. A. Koster, V. D. Mihailetschi, R. Ramaker, P. W. M. Blom, *Appl. Phys. Lett.* **2005**, *86*, 123509.
- [46] C. M. Proctor, M. Kuik, T.-Q. Nguyen, *Prog. Polym. Sci.* **2013**, *38*, 1941.
- [47] C. M. Proctor, T.-Q. Nguyen, *Appl. Phys. Lett.* **2015**, *106*, 083301.
- [48] K. Vandewal, J. Benduhn, V. C. Nikolis, *Sustainable Energy Fuels* **2018**, *2*, 538.
- [49] K. Vandewal, K. Tvingstedt, A. Gadisa, O. Inganäs, J. V. Manca, *Phys. Rev. B* **2010**, *81*, 125204.

- [50] S. M. Menke, A. Sadhanala, M. Nikolka, N. A. Ran, M. K. Ravva, S. Abdel-Azeim, H. L. Stern, M. Wang, H. Sirringhaus, T.-Q. Nguyen, J.-L. Brédas, G. C. Bazan, R. H. Friend, *ACS Nano* **2016**, *10*, 10736.
- [51] N. A. Ran, S. Roland, J. A. Love, V. Savikhin, C. J. Takacs, Y.-T. Fu, H. Li, V. Coropceanu, X. Liu, J.-L. Brédas, G. C. Bazan, M. F. Toney, D. Neher, T.-Q. Nguyen, *Nat. Commun.* **2017**, *8*, 79.
- [52] S. M. Tuladhar, M. Azzouzi, F. Delval, J. Yao, A. A. Y. Guilbert, T. Kirchartz, N. F. Montcada, R. Dominguez, F. Langa, E. Palomares, J. Nelson, *ACS Energy Lett.* **2016**, *1*, 302.
- [53] K. D. Rosenthal, M. P. Hughes, B. R. Luginbuhl, N. A. Ran, A. Karki, S.-J. Ko, H. Hu, M. Wang, H. Ade, T.-Q. Nguyen, *Adv. Energy Mater.* **2019**, *9*, 1901077.
- [54] U. Rau, *Phys. Rev. B* **2007**, *76*, 085303.
- [55] M. Babics, T. Duan, A. H. Balawi, R.-Z. Liang, F. Cruciani, I.-D. Carja, D. Gottlieb, I. McCulloch, K. Vandewal, F. Laquai, P. M. Beaujuge, *ACS Appl. Energy Mater.* **2019**, *2*, 2717.
- [56] T. M. Burke, S. Sweetnam, K. Vandewal, M. D. McGehee, *Adv. Energy Mater.* **2015**, *5*, 1500123.
- [57] V. C. Nikolis, A. Mischok, B. Siegmund, J. Kublitski, X. Jia, J. Benduhn, U. Hörmann, D. Neher, M. C. Gather, D. Spoltore, K. Vandewal, *Nat. Commun.* **2019**, *10*, 3706.
- [58] W. Shockley, H. J. Queisser, *J. Appl. Phys.* **1961**, *32*, 510.
- [59] J. Benduhn, K. Tvingstedt, F. Piersimoni, S. Ullbrich, Y. Fan, M. Tropiano, K. A. McGarry, O. Zeika, M. K. Riede, C. J. Douglas, S. Barlow, S. R. Marder, D. Neher, D. Spoltore, K. Vandewal, *Nat. Energy* **2017**, *2*, 17053.
- [60] S. Ullbrich, J. Benduhn, X. Jia, V. C. Nikolis, K. Tvingstedt, F. Piersimoni, S. Roland, Y. Liu, J. Wu, A. Fischer, D. Neher, S. Reineke, D. Spoltore, K. Vandewal, *Nat. Mater.* **2019**, *18*, 459.
- [61] X.-K. Chen, M. K. Ravva, H. Li, S. M. Ryno, J.-L. Brédas, *Adv. Energy Mater.* **2016**, *6*, 1601325.
- [62] K. Vandewal, K. Tvingstedt, O. Inganäs, *Phys. Rev. B* **2012**, *86*, 035212.
- [63] M. Bixon, J. Jortner, J. W. Verhoeven, *J. Am. Chem. Soc.* **1994**, *116*, 7349.
- [64] V. Nádaždy, F. Schauer, K. Gmucová, *Appl. Phys. Lett.* **2014**, *105*, 142109.
- [65] F. Schauer, M. Tkáčová, V. Nádaždy, K. Gmucová, M. Ožvoldová, L. Tkáč, J. Chlupík, *Polym. Degrad. Stab.* **2016**, *126*, 204.
- [66] S. D. Collins, C. M. Proctor, N. A. Ran, T.-Q. Nguyen, *Adv. Energy Mater.* **2016**, *6*, 1501721.
- [67] D. Venkateshvaran, M. Nikolka, A. Sadhanala, V. Lemaury, M. Zelazny, M. Kepa, M. Hurhangee, A. J. Kronemeijer, V. Pecunia, I. Nasrallah, I. Romanov, K. Broch, I. McCulloch, D. Emin, Y. Olivier, J. Cornil, D. Beljonne, H. Sirringhaus, *Nature* **2014**, *515*, 384.
- [68] S. Hood, N. Zarrabi, P. Meredith, I. Kassal, A. Armin, *J. Phys. Chem. Lett.* **2019**, *10*, 3863.
- [69] R. Englman, J. Jortner, *Mol. Phys.* **1970**, *18*, 145.
- [70] M. E. Ziffer, S. B. Jo, H. Zhong, L. Ye, H. Liu, F. Lin, J. Zhang, X. Li, H. W. Ade, A. K.-Y. Jen, D. S. Ginger, *J. Am. Chem. Soc.* **2018**, *140*, 9996.
- [71] Y. Zhong, M. T. Trinh, R. Chen, G. E. Purdum, P. P. Khlyabich, M. Sezen, S. Oh, H. Zhu, B. Fowler, B. Zhang, W. Wang, C.-Y. Nam, M. Y. Sfeir, C. T. Black, M. L. Steigerwald, Y.-L. Loo, F. Ng, X.-Y. Zhu, C. Nuckolls, *Nat. Commun.* **2015**, *6*, 8242.
- [72] Y. Tamai, Y. Fan, V. O. Kim, K. Ziabrev, A. Rao, S. Barlow, S. R. Marder, R. H. Friend, S. M. Menke, *ACS Nano* **2017**, *11*, 12473.
- [73] S. Gélinas, A. Rao, A. Kumar, S. L. Smith, A. W. Chin, J. Clark, T. S. van der Poll, G. C. Bazan, R. H. Friend, *Science* **2014**, *343*, 512.
- [74] B. R. Gautam, R. Younts, J. Carpenter, H. Ade, K. Gundogdu, *J. Phys. Chem. A* **2018**, *122*, 3764.
- [75] A. K. K. Kyaw, D. H. Wang, D. Wynands, J. Zhang, T.-Q. Nguyen, G. C. Bazan, A. J. Heeger, *Nano Lett.* **2013**, *13*, 3796.
- [76] V. V. Brus, *Org. Electron.* **2016**, *29*, 1.
- [77] V. V. Brus, C. M. Proctor, N. A. Ran, T.-Q. Nguyen, *Adv. Energy Mater.* **2016**, *6*, 1502250.
- [78] C. M. Proctor, C. Kim, D. Neher, T.-Q. Nguyen, *Adv. Funct. Mater.* **2013**, *23*, 3584.
- [79] J. Vollbrecht, V. V. Brus, S.-J. Ko, J. Lee, A. Karki, D. X. Cao, K. Cho, G. C. Bazan, T.-Q. Nguyen, *Adv. Energy Mater.* **2019**, *9*, 1901438.
- [80] S. Albrecht, J. R. Tumbleston, S. Janietz, I. Durnsch, S. Allard, U. Scherf, H. Ade, D. Neher, *J. Phys. Chem. Lett.* **2014**, *5*, 1131.
- [81] B. P. Rand, D. Cheyons, K. Vasseur, N. C. Giebink, S. Mothy, Y. Yi, V. Coropceanu, D. Beljonne, J. Cornil, J.-L. Brédas, J. Genoe, *Adv. Funct. Mater.* **2012**, *22*, 2987.
- [82] S. Mukherjee, C. M. Proctor, G. C. Bazan, T.-Q. Nguyen, H. Ade, *Adv. Energy Mater.* **2015**, *5*, 1500877.
- [83] T. M. Burke, M. D. McGehee, *Adv. Mater.* **2014**, *26*, 1923.
- [84] Y. Yi, V. Coropceanu, J.-L. Brédas, *J. Am. Chem. Soc.* **2009**, *131*, 15777.
- [85] Y. Liu, J. Zhao, Z. Li, C. Mu, W. Ma, H. Hu, K. Jiang, H. Lin, H. Ade, H. Yan, *Nat. Commun.* **2014**, *5*, 5293.
- [86] B. A. Collins, Z. Li, J. R. Tumbleston, E. Gann, C. R. McNeill, H. Ade, *Adv. Energy Mater.* **2013**, *3*, 65.
- [87] L. Ye, S. Li, X. Liu, S. Zhang, M. Ghasemi, Y. Xiong, J. Hou, H. Ade, *Joule* **2019**, *3*, 443.
- [88] M. Alla, E. Lippmaa, *Chem. Phys. Lett.* **1982**, *87*, 30.
- [89] A. J. Robbins, W. T. K. Ng, D. Jochym, T. W. Keal, S. J. Clark, D. J. Tozer, P. Hodgkinson, *Phys. Chem. Chem. Phys.* **2007**, *9*, 2389.
- [90] M. P. Hanrahan, A. Venkatesh, S. L. Carnahan, J. L. Calahan, J. W. Lubach, E. J. Munson, A. J. Rossini, *Phys. Chem. Chem. Phys.* **2017**, *19*, 28153.
- [91] D. H. Barich, J. M. Davis, L. J. Schieber, M. T. Zell, E. J. Munson, *J. Pharm. Sci.* **2006**, *95*, 1586.
- [92] M. R. Hansen, R. Graf, H. W. Spiess, *Chem. Rev.* **2016**, *116*, 1272.
- [93] S. R. Chaudhari, J. M. Griffin, K. Broch, A. Lesage, V. Lemaury, D. Dudenko, Y. Olivier, H. Sirringhaus, L. Emsley, C. P. Grey, *Chem. Sci.* **2017**, *8*, 3126.
- [94] K. Saalwächter, H. W. Spiess, in *Polymer Science: A Comprehensive Reference*, (Eds: K. Matyjaszewski, M. Möller), Vol. 2, Elsevier, Amsterdam **2012**, pp. 185–219.
- [95] I. Schnell, H. W. Spiess, *J. Magn. Reson.* **2001**, *151*, 153.
- [96] M. Feike, D. E. Demco, R. Graf, J. Gottwald, S. Hafner, H. W. Spiess, *J. Magn. Reson., Ser. A* **1996**, *122*, 214.
- [97] M. R. Hansen, R. Graf, H. W. Spiess, *Acc. Chem. Res.* **2013**, *46*, 1996.
- [98] R. C. Nieuwendaal, C. R. Snyder, D. M. DeLongchamp, *ACS Macro Lett.* **2014**, *3*, 130.
- [99] R. Nieuwendaal, in *NMR Methods for Characterization of Synthetic and Natural Polymers*, (Eds: R. Zhang, T. Miyoshi, P. Sun), Royal Society of Chemistry, London, UK **2019**, Ch.15, pp. 325–362.
- [100] H. Ivanir-Dabora, E. Nimerovsky, P. K. Madhu, A. Goldbourt, *Chem. - Eur. J.* **2015**, *21*, 10778.
- [101] E. R. de Azevedo, K. Saalwächter, O. Pascui, A. A. de Souza, T. J. Bonagamba, D. Reichert, *J. Chem. Phys.* **2008**, *128*, 104505.
- [102] K. Schäler, A. Achilles, R. Bärenwald, C. Hackel, K. Saalwächter, *Macromolecules* **2013**, *46*, 7818.
- [103] L. A. Straasø, Q. Saleem, M. R. Hansen, in *Annual Reports on NMR Spectroscopy*, (Ed: G. A. Webb), Academic Press, San Diego, CA **2016**, pp. 307–383.